Spin and orbital moment in amorphous $Co_{68}Fe_{24}Zr_8$ layers

Thomas Hase,[1] Hossein Raanaei,[2,3] Hans Lidbaum,[4] Cecilia Sánchez-Hanke,[5] Stuart Wilkins,[6] Klaus Leifer,[4] and Björgvin Hjörvarsson[2,*]

[1]*Department of Physics, University of Warwick, Coventry CV4 7AL, United Kingdom*

[2]*Department of Physics and Materials Science, Uppsala University, P.O. Box 530, 751 21 Uppsala, Sweden*

[3]*Department of Physics, Persian Gulf University, Bushehr 75168, Iran*

[4]*Institute of Electron Microscopy and Nano-Engineering, Uppsala University, P.O. Box 534, SE 751 21 Uppsala, Sweden*

[5]*National Synchrotron Light Source, Brookhaven National Laboratory, Upton, New York 11973, USA*

[6]*Department of CMPMSD, Brookhaven National Laboratory, Upton, New York 11973, USA*

(Received 17 July 2009; revised manuscript received 4 September 2009; published 1 October 2009)

The ratio of the orbital to the spin magnetic moment was determined for both Fe and Co in amorphous $Co_{68}Fe_{24}Zr_8$ layers using x-ray circular dichroism. The investigations were performed on both thick $Co_{68}Fe_{24}Zr_8$ layers as well as on amorphous $Co_{68}Fe_{24}Zr_8/Al_{70}Zr_{30}$ multilayers grown by dc sputtering. Structural characterization was performed using x-ray reflectometry, x-ray diffraction, and transmission electron microscopy. X-ray circular dichroism, x-ray magnetic scattering as well as the magneto-optic Kerr effect were used to characterize the magnetic properties of the amorphous materials. The ratio of the orbital to spin moments in the single CoFeZr-layer sample was 0.012 ± 0.005 for Fe and 0.078 ± 0.005 for Co. Substantial reduction in the the ratio of the orbital to spin moments was observed with decreasing CoFeZr-layer thickness.

DOI: 10.1103/PhysRevB.80.134402 PACS number(s): 75.70.Ak, 75.50.Kj, 68.65.Ac, 75.30.Gw

I. INTRODUCTION

The physical properties of amorphous materials are only partially understood and there are currently no theoretical calculations which can be used to predict their properties from first principles. Amorphous materials are relatively common while most of their physical properties are much less known than their crystalline counterparts. The magnetic properties are no exception, although amorphous magnetic materials are widely used.[1,2] Furthermore, there exists even counter intuitive properties which are often utilized but poorly understood. One such example is the field-induced anisotropy of amorphous magnets.[3,4] The local anisotropy, seen as a spatially varying anisotropy in thin amorphous films, can be argued to have the same origin.

The relationship between the spin and orbital components of the magnetic moment are fundamental for the understanding of both the macroscopic and microscopic properties of magnetic materials. Spin-orbit coupling can be viewed as the source of magnetic anisotropy and so the local symmetry of the atomic arrangements plays an important role in determining the observed anisotropy. The atomic arrangement within a material is often linked intimately to the underlying lattice in a crystal structure and is reflected in the term crystalline anisotropy, which is one of the basic parameters used to describe magnetic materials. In amorphous materials magnetocrystalline anisotropy must be absent due to the lack of long-range order but a macroscopic magnetic anisotropy is still observed. Although there is no long-range order, variation in the local arrangement of atoms on the nanometer range appears to be sufficient to break the local symmetry and thereby give rise to the anisotropy observed in amorphous materials.[5,6] Thus, although the long-range crystalline order is absent, the local atomic arrangement allows for the creation of easy and hard magnetic axes within amorphous magnetic materials which can be further modified through, for example, ion implantation.[7,8]

The orbital moments in bulk materials of high symmetry within crystalline solids are strongly reduced due to orbital quenching. However, they may attain large values when the dimensionality is reduced. In contrast to crystalline materials, thin films of amorphous magnetic alloys show large variations in both the spin and angular momentum as a function of both composition and dimensionality. Thus, a detailed understanding of the interplay between the magnetic and structural properties of solids is required for the tailoring of magnetic properties such as interface magnetism in new artificial amorphous magnetic systems.[9]

X-ray magnetic circular dichroism (XMCD) allows the element-specific determination of the orbital and spin magnetic moments[10,11] and thereby provides a direct route for exploring the element-specific contribution to the magnetic properties in materials.[12–16] In this paper we address the orbit to spin ratio (m_{orbit}/m_{spin}) of the magnetic moment of both Fe and Co in amorphous CoFeZr magnetic layers using XMCD. The thickness dependence of m_{orbit}/m_{spin} is also addressed and the interface contribution as well as the element-specific contributions to the magnetic properties of CoFeZr are discussed.

II. EXPERIMENT

A series of samples were grown using dc magnetron sputtering on naturally oxidized Si(111) substrates, which were annealed at 530 °C for one hour prior to deposition. The base pressure of the chamber was below 2×10^{-9} Torr. During the deposition of the layers, Ar gas with a purity of 99.9999% was kept at a pressure of 3.0×10^{-3} Torr. CoFeZr layers were deposited from a single composite target with a nominal composition of $Co_{60}Fe_{25}Zr_{15}$ while the $Al_{70}Zr_{30}$ layers were grown by codeposition from two elemental sources. All the samples were grown on a nominally 30 Å thick $Al_{70}Zr_{30}$ buffer layer at room temperature and were capped

by aluminum to prevent oxidation of the magnetically active layers.

Here we discuss the results from two sets of samples. The first sample contains a single CoFeZr layer and has a nominal structure: $Si/SiO_2/CoFeZr(200\ \text{Å})$. We compare this single thick layer with a second series of multilayer samples consisting of ten repeats of a bilayer with varying CoFeZr thickness. The nominal structure of the multilayers are $Si/SiO_2/AlZr(30\ \text{Å})/[CoFeZr(X\ \text{Å})/AlZr(30\ \text{Å})]\times 10$, with $X=10$, 20, and 30 Å, these are labeled as sample 10/30, 20/30, and 30/30, respectively. For both sets of samples a 20 Å aluminum capping layer protects the underlying magnetic material by forming a passivating layer of oxidized aluminum. The chemical composition of the samples was confirmed using Rutherford backscattering spectrometry while the amorphous nature of the samples was investigated by using x-ray diffraction and transmission electron microscopy (TEM). For the high-resolution TEM (HRTEM) studies a FEI Tecnai F30ST microscope operating at 300 kV was used. Electron diffraction was performed on a JEOL JEM-2000FXII instrument using an electron-beam energy of 200 kV.

Layer and interface parameters were determined using grazing-incidence scattering techniques. Specular reflectivity and diffuse scattering were recorded on station X22C at the National Synchrotron Light Source (NSLS) at Brookhaven National Laboratory. A silicon (111) monochromator was used to provide a beam of energy 8.8 keV which was focused vertically onto the sample using a mirror and slits with dimensions 150 μm$\times$1 mm. The scattered radiation was measured using a slit-collimated scintillator detector with a resolution matched to the incident beam.

The bulk magnetization of the samples was determined though magneto-optical Kerr effect (MOKE) measurements recorded at room temperature using a longitudinal geometry with polarized light. Element-specific magnetic information was recorded using XMCD and x-ray resonant magnetic scattering (XRMS) on beamline X13A at the NSLS. An elliptical polarizing wiggler produces radiation covering the L edges of the transition metals of interest. The polarization of the incident light was switched at 22 Hz and a phase-sensitive detection system using lock-ins was employed to record simultaneously the magnetic and charge signals by measuring at 22 and 44 Hz, respectively. The sample was mounted in a high-vacuum two-circle diffractometer and the experiment was conducted in a horizontal scattering geometry. The sample was magnetized *in situ* using an electromagnet with a maximum field of 20 mT applied parallel to the sample surface. The drain current from the sample was measured by affixing a thin wire to the sample surface. The reflected intensity was recorded using an avalanche photodiode with a digital counting chain synchronized to the helicity reversals.

III. RESULTS

A. Structural and compositional characterization

In this section we elucidate the layer thicknesses and interface morphologies using grazing-incidence reflectivity.

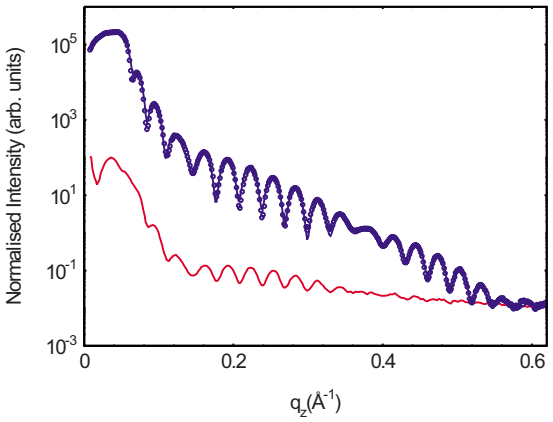

FIG. 1. (Color online) Specular reflectivity (upper curve) and longitudinal diffuse scan (lower curve) for the single 200 Å CoFeZr layer. The specular data (circles) are well fitted (line) for all scattering vectors. The fringes observed in the specular data are replicated in the longitudinal diffuse data recorded with a sample offset of −0.1°, clearly illustrating that vertical correlations exist in the topological roughness that extend over the entire sample thickness.

The q vectors that are probed in such a geometry are insensitive to the crystal structure of the material. Representative reflectivity data is shown in Fig. 1 for the single CoFeZr film. The forward diffuse scatter has been removed prior to fitting by subtracting the longitudinal diffuse data which was recorded with an offset in the sample angle of −0.1° from the specular condition. The reflectivity has been fitted using a generic algorithm to minimize the difference between the data and a model structure using the GenX code.[17] Excellent agreement between simulation and data has been achieved with the periodicity and amplitude of the reflectivity fringes being well reproduced in the simulation. The fitted CoFeZr-layer thickness is close to the nominal value, 202.0 ± 0.1 Å with an interface width of 4.7 ± 0.1 Å. The aluminum capping layer was deduced to be close to fully oxidized with a fitted thickness of 27.3 ± 0.2 Å and a surface roughness 5.1 ± 0.2 Å identical to both the substrate (4.6 ± 0.4 Å) and CoFeZr layers. The relative concentration of the constituents of the CoFeZr layer was determined from Ruherford backscattering spectrometry measurements which yielded a layer composition of $Co_{68}Fe_{24}Zr_8$ which was in excellent agreement with the refined CoFeZr electron density determined from the specular reflectivity fit.

The longitudinal diffuse data shown in Fig. 1 shows fringes with the same periodicity as those found in the specular data. This is indicative of a high degree of vertical correlation in the roughness which extends from the substrate through to the sample surface. As the amplitude of the interface width for all interfaces is similar, we can conclude that much of the topological roughness is correlated. The amplitude of the topological roughness can be estimated by considering the ratio of the integrated specular to diffuse scatter in a transverse diffuse scan. Such a scan recorded at $q_z=0.222\ \text{Å}^{-1}$ is shown in Fig. 2 and a lower limit on the amplitude of the topological roughness is 1.0 ± 0.2 Å. From the rather large discrepancy between the specular and diffuse

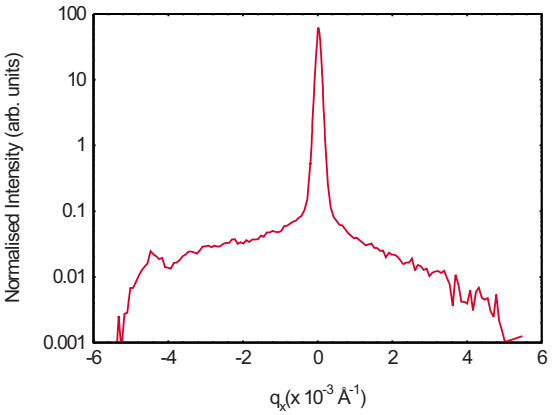

FIG. 2. (Color online) Transverse diffuse, or rocking curve, for the 200 Å single-layer CoFeZr sample. The data were recorded at a fixed out-of-plane scattering vector of q_z=0.222 Å^{-1}. The specular ridge at q_x=0 is broadened as a result of roughness on a large lateral length scale. From the ratio of the specular and diffuse scatter a lower limit for the amplitude of the topological roughness is 1.0±0.2 Å.

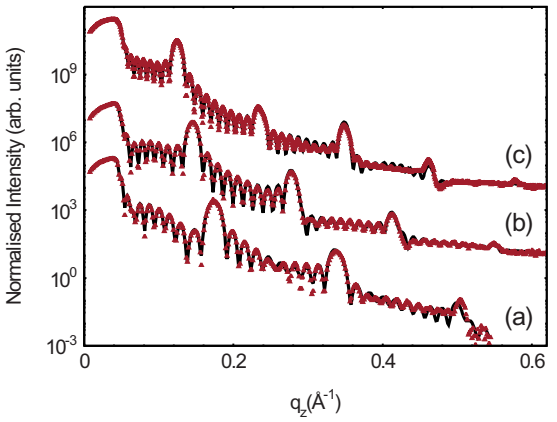

FIG. 3. (Color online) Specular reflectivity for the multilayer samples. Sequential curves have been offset by decades of intensity for clarity. The multilayer peak positions correspond to fitted bilayer thicknesses of 39.3±0.1 Å, 47.9±0.1 Å, and 57.3±0.5 Å for samples 10/30, 20/30, and 30/30, respectively. The solid lines are simulated fits to the data (circles).

analysis we conclude that the interface contains significant interdiffusion between the layers. This is in agreement with our previous study of similar amorphous material.[4] It is worth noting that the width of the specular ridge at q_x=0 in Fig. 2 is considerably broader [$(2.5\pm0.3)\times10^{-4}$ Å^{-1}] than the instrumental resolution [$(3.2\pm0.1)\times10^{-5}$ Å^{-1}]. This shows that there exist some large in-plane structural features that are beyond the coherence length of the x-ray beam (which at this scattering vector is approximately 20 μm). These are most likely to be associated with large terraces commonly observed on Si(111) substrates.

Incorporating the CoFeZr amorphous materials into magnetic heterostructures composed of repeated bilayers of thin CoFeZr and amorphous AlZr does not significantly alter the structural parameters. The reflectivity curves for samples 10/30, 20/30, and 30/30 with increasing CoFeZr thickness are shown in Fig. 3. A summary of the layer thicknesses and roughness derived from the fits are presented in Table I.

As in the case of the single CoFeZr film, the layer thicknesses are close to the nominal values and the interface widths are low. We note that the roughness of the AlZr/CoFeZr and CoFeZr/AlZr interfaces are asymmetric. The roughness of the CoFeZr/AlZr interface decreases somewhat with increasing CoFeZr thickness, see Table I. As was the case for the single-layer sample, fringes are observed in the longitudinal diffuse scans that match features in the specular scans for all multilayer samples, clearly demonstrating that the topological roughness is strongly correlated between the layers. The length scales over which these correlations extend can be extracted from a full reciprocal space map of the diffuse data which is shown for the sample 20/30 in Fig. 4. The diffuse data is clearly confined to strong streaks of diffuse scatter that occur at the out-of-plane reciprocal space, q_z, positions corresponding to the low-angle multilayer peaks seen in Fig. 3. The broad extension in q_x of the diffuse Bragg sheets shows that the frequency components of the roughness that are correlated over a single bilayer extend down to a length scale less than 500 Å. The slight curvature of the Bragg sheets at high q_x is caused by refraction effects when either the incident or exit beams correspond to the critical angle. Apart from the broadened specular ridge that was seen in Fig. 2, the transverse rocking curves recorded at the Bragg peaks are rather flat (consistent with a short in-plane correlation length) and give a lower limit for the correlated topological roughness of 0.8±0.2 Å in excellent agreement with the single-layer sample. The strong correlation of the interface morphology between the layers can also be seen in the HRTEM images shown in Fig. 5 where the waviness of the layers is well replicated from the substrate to the surface. A clear example is seen by a typical cusp can be seen in Fig. 5(b), indicated by a white arrow. Note how the cusp causes a change in the interface morphology which subsequently propagates throughout the remainder of the stack while preserving the bilayer thickness between the layers.

Diffraction and microscopy studies confirm the amorphous structure of both the CoFeZr and AlZr layers. High-resolution TEM images of the thinnest, 10/30, and thickest multilayer sample, 30/30, in cross section are shown in Figs. 5(a) and 5(b), respectively. The silicon substrates were oriented close to the [110] zone axis in order to have the electron beam parallel with the deposited layers. Both samples exhibit amorphous multilayer structure, although with some interface intermixing between the layers as well as correlated

TABLE I. Average bilayer thicknesses and AlZr thicknesses of the samples 10/30, 20/30, and 30/30 accompanied by AlZr and CoFeZr roughnesses are determined from simulations of the x-ray reflectivity curves.

Parameter	Sample 10/30 (Å)	Sample 20/30 (Å)	Sample 30/30 (Å)
Bilayer thickness	39.3±0.1	47.9±0.1	57.3±0.5
AlZr	29.8±0.5	28.3±0.5	29.8±0.2
CoFeZr roughness	5.5±0.1	6.09±0.08	7.8±0.2
AlZr roughness	11±1	7.6±0.3	6.3±0.1

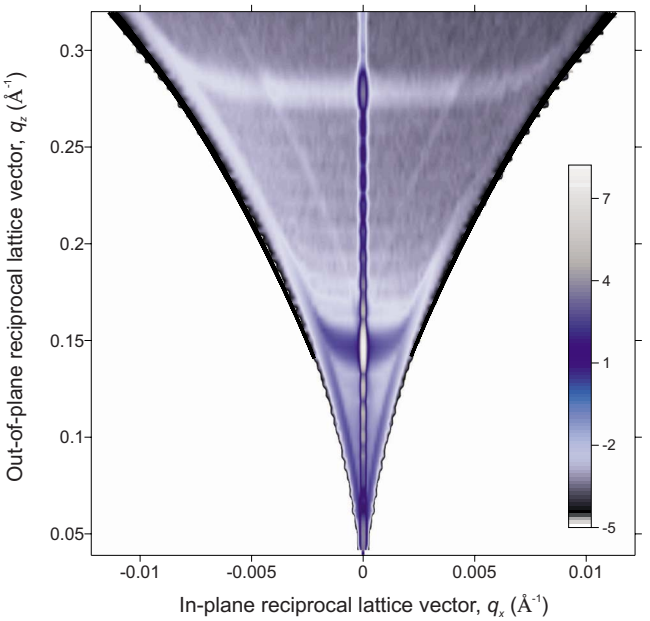

FIG. 4. (Color online) Full reciprocal space map of the diffuse scattering data from sample 20/30. Data is presented on a logarithmic scale. The diffuse scattering is predominantly found in streaks at the out-of-plane scattering vectors of the multilayer peaks seen in the specular scans shown in Fig. 3. The slight curvature of the Bragg sheets at high q_x is caused by refraction effects when either the incident or exit beams are at the critical angle.

waviness. Note that the aluminum cap layer of the thinnest sample shows crystalline lattice fringes, thus the capping is not fully oxidized in this sample.

To further confirm the amorphous structure of the layers, selected area electron-diffraction patterns (SAED) were acquired in top-view sample geometry. The silicon substrate was oriented to have the electron beam in the [111] zone-axis direction and illuminating a region of approximately 2.1 μm in diameter. A SAED pattern of the thinnest sample, 10/30 is shown in Fig. 6. The well-defined spot pattern originates from the silicon substrate while the broad rings come from the amorphous material within the sample. At a diffraction angle corresponding to a lattice spacing of approximately 1.44 Å a sharp ring is observed which corresponds to the (220) atomic planes in face-centered-cubic aluminum, which from Fig. 5 were also found in the cap layer. The intensity of the crystalline cap layer is barely visible since the diffracting volume is small and will be superimposed with the amorphous bands of the CoFeZr and AlZr. The expected positions of the (111), (200), (220), and (113) reflections in Al are indicated with white arrows in Fig. 6. The composition of the magnetic material was determined by Rutherford backscattering and is reported in more detail in our previous work[4] and is $Co_{68}Fe_{24}Zr_8$.

B. Magnetic characterization

The field dependence of the magnetization for the 200 Å thick sample is shown in Fig. 7. The measurements were performed at room temperature, using the magneto-optical

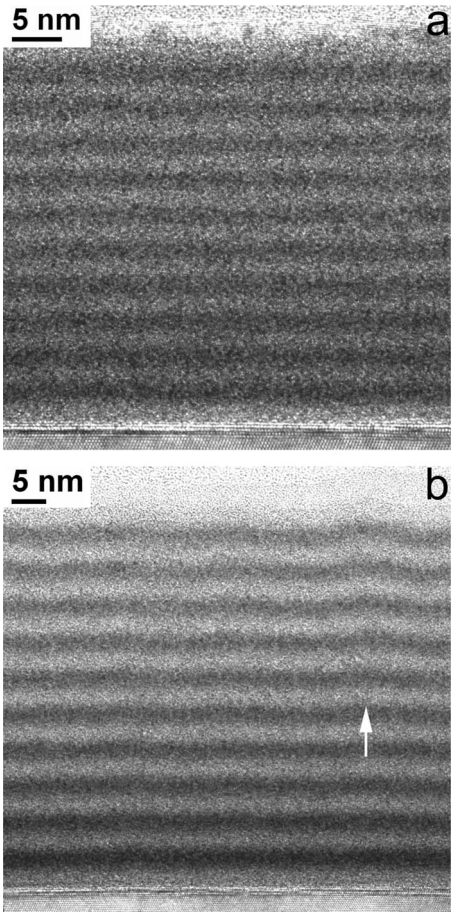

FIG. 5. High-resolution TEM images of the CoFeZr/AlZr multilayer samples in cross-sectional view. The sample with the thinnest CoFeZr-layer thickness, 10/30 is shown in (a). An amorphous structure is observed throughout the deposited material, except for the Al cap layer at the top. In (b) the sample with the thickest CoFeZr layer, 30/30, is shown. The white arrow indicates a region where the interface morphology is changed which then propagates throughout the remainder of the multilayers. The silicon substrate is seen at the bottom of each image.

Kerr effect. As seen in Fig. 7, the sample appear to be ferromagnetic, with a coercivity of about 1 mT. After some rounding at low fields the sample is fully saturated by about 5 mT. The sample is magnetically isotropic in the plane as both the saturation and coercive fields are independent of the alignment of the sample in the applied field. The reduction in the magnetization at the lowest fields originates from the randomness in the local anisotropy of the layers. The effect of the randomness in the local anisotropy can be seen as wandering axes of the direction of the magnetization which has been observed by magnetic imaging for fields below the saturation value.[4]

The element-specific magnetization was obtained using resonant x rays. Unlike optical probes which interrogate the average magnetic moment within their sample depth, resonant x rays can be used to extract the element-specific magnetic response when tuned to an appropriate energy. X-ray absorption (XAS) and XMCD have become standard tools in characterizing magnetic materials. For the transition materi-

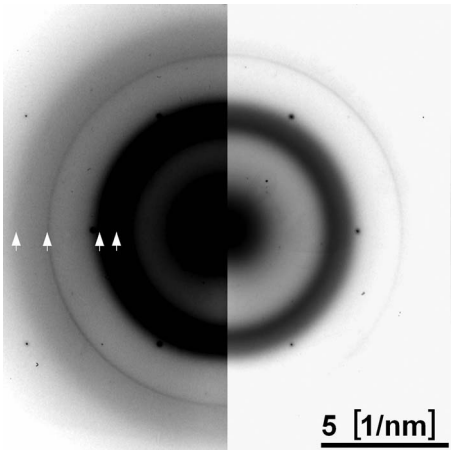

FIG. 6. Selected area electron-diffraction pattern in the TEM from the 10 Å CoFeZr multilayer sample in top-view geometry, acquired including a part of the silicon substrate (spot pattern). Broad dark bands indicates an amorphous structure of the CoFeZr and AlZr layers. The sharp ring at approximately 1.44 Å correspond to polycrystalline Al 220 planes, originating from the cap layer (see Fig. 5). White arrows indicate the expected spacing of (111), (200), (220), and (113) reflections in Al. The brightness of the left-hand and right-hand parts of the image is different for enhancing the dynamic range in the figure and the intensity scale was inverted for clarity.

als the resonant transition of interest occurs at the L_3 and L_2 edges because the absorption is between the $2p$ core level and the unoccupied but spin-polarized $3d$ states.

Both Fe and Co loops recorded in reflection are identical and are illustrated in Fig. 8. The Fe and Co are therefore ferromagnetically aligned and rotate coherently with the applied field. The noise on the Fe signal is larger than that observed from the Co due to the significantly lower Fe concentration. The coercive field obtained from the x-ray measurements is somewhat larger than obtained from the MOKE measurements which can be traced to the remnant field in the magnet used in the x-ray measurements. The obtained saturation field is in excellent agreement with that obtained by MOKE, about 5 mT. At this field the importance of the slight offset from the remnant field from the magnet has diminished. Thus the MOKE and the XRMS measurements are consistent, when considering the experimental uncertainties.

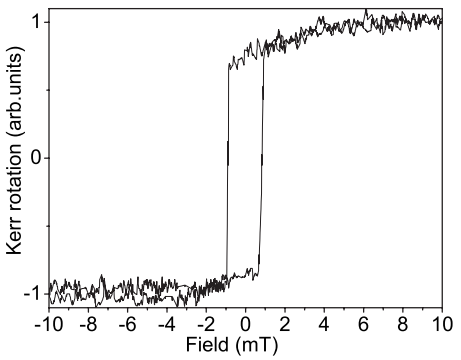

FIG. 7. Room-temperature magnetization as a function of applied field recorded using the magneto-optical Kerr rotation effect.

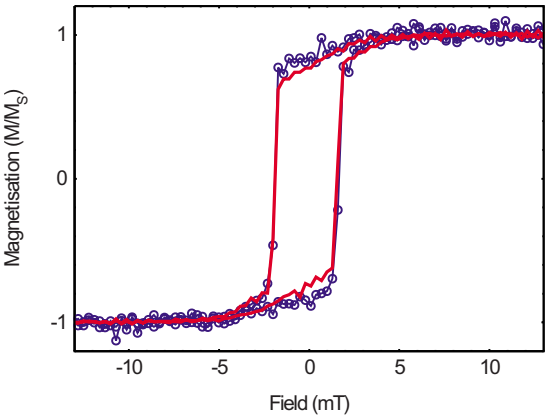

FIG. 8. (Color online) The difference in the reflected signal as a function of applied field for the single-layer sample. The Fe (circles and line) and Co (line) loops are similar within experimental error and show a coercive field of 1.7 ± 0.1 mT.

The absorption of circular polarized light that gives rise to the XMCD signal obeys the so-called sum rules, derived assuming electric dipole transitions only. The orbital component of the magnetization contributes with the same sign to the XMCD signal in a ratio 2:1 at the L_3 and L_2 edges, respectively. The spin component arises from the core-hole splitting of the $2p$ states due to the spin-orbit interaction and the $3d$ spin moment contributes equally to the two edges but with opposite sign. Thus by considering the integrals under the XMCD curves at the two edges, the spin and orbital components of the magnetic moment, can, in principal, be determined as

$$m_{spin} = -\frac{1}{C}(A - 2B)\mu_B, \tag{1a}$$

$$m_{orbit} = -\frac{2}{3C}(A + B)\mu_B. \tag{1b}$$

In Eqs. (1a) and (1b) A is the integral of the XMCD signal across the L_3 edge and similarly B is the integral across the L_2 edge. The constant C is element specific and contains the number of holes per unit area and the exact polarization of the incident photons.

The absorption spectra were recorded using the electron yield method in a fixed saturating field of ± 10 mT from a wire attached to the surface of the film. Data was recorded using a lock-in measuring at twice the helciity switching frequency at a sample angle of 30°. In order to remove artifacts introduced by the applied field the data from the two fields was averaged. The resulting normalized XAS spectra across the L_3 and L_2 edges of Fe and Co for the thick single film are shown in Fig. 9. Following standard procedures the background in the pre-edge region has been removed and the step height normalized to unity well above the L_2 edge. In Fig. 10 we show the difference data which was recorded simultaneously with the absorption data by measuring the electron yield at the helicity switching frequency. The difference peaks at both the L_3 and L_2 edges of Co are larger than those at the Fe edges showing that the moment of the

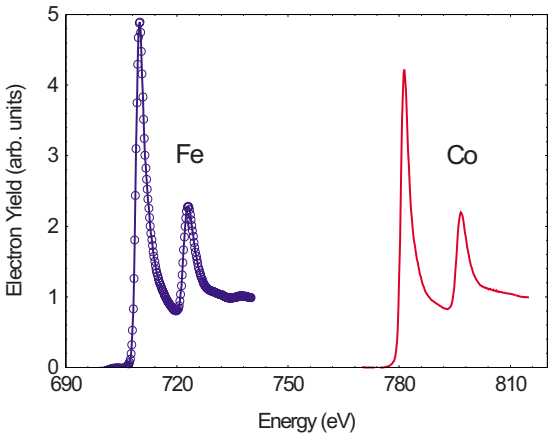

FIG. 9. (Color online) Electron yield as a function of energy across the Fe (circles and line) and Co (line) L_3 and L_2 edges for the single 200 Å CoFeZr film. The absorption data is an average of two curves collected under opposite but saturating fields and has been normalized to give a step height of unity across the two edges.

CoFeZr is concentrated on Co. Scanning the photon energy across the Zr L edges showed XAS features but no evidence of any polarization on the Zr.

The integral terms A and B were obtained by calculating the cumulative integral of the difference data as a function of energy across the two edges. From Eq. (1a), it is clear that the orbital moment is proportional to the sum of A and B. From the shape of the cumulative integral in Fig. 10 it is clear that the orbital moment on the Fe sites is nearly quenched while there remains a considerable orbital component on the Co. As the element-specific constant in Eqs. (1a) and (1b) was not known, it was not possible to extract the specific spin and orbital components but the ratio is independent of C and can be determined easily. For Fe, the ratio of the orbital to spin moments is 0.012 ± 0.005 and for Co, is 0.078 ± 0.005 for the single CoFeZr-layer sample. Thus, the contribution to the orbital moment is dominated by the Co contribution.

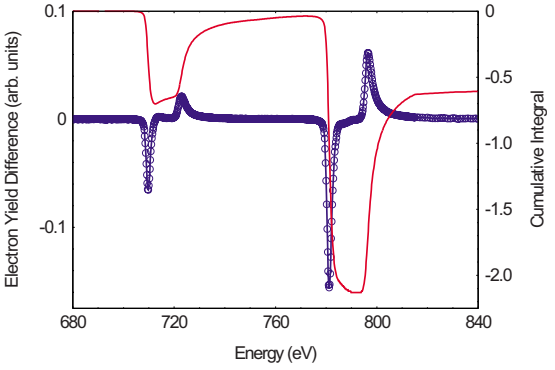

FIG. 10. (Color online) The difference in electron yield as a function of energy across the Fe and Co edges (circles and line) and the cumulative integral of the difference signal (line) for the single CoFeZr film. The data was recorded simultaneously with the absorption signals shown in Fig. 9. Artifacts associated with recording the electron yield in a field have been removed by averaging two curves collected under opposite but saturating fields. No normalization or correction terms have been applied to the data.

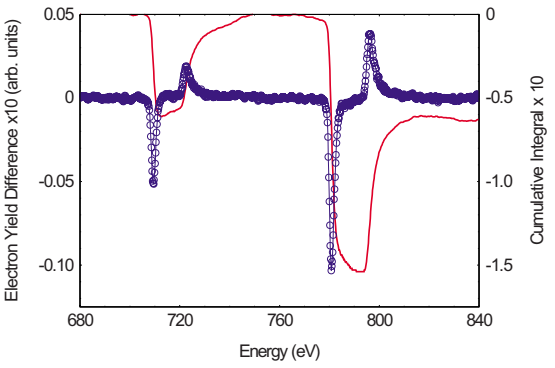

FIG. 11. (Color online) The difference in electron yield as a function of energy across the Fe and Co edges (circles and line) and the cumulative integral of the difference signal (line) for the 30/30 multilayered sample. The data treatment is identical to that applied to the data in Fig. 10. The lower signal to noise arises from the thickness of the effective capping layer which is the sum of the protective alumina layer and the top AlZr layer of the bilayer.

When the magnetic CoFeZr layer is in a multilayer the data trends are remarkably similar. No difference between the multilayer samples was observed and we show in Fig. 11 representative data for sample 30/30. The data is considerably noisier than that obtained for a single layer, primarily due to the increased depth of the magnetic layer. The detected electrons have to penetrate both the cap of the partially oxidized alumina and the top AlZr layer in the multilayered structures. Again it is clear that the Fe orbital moment is quenched. The ratio of the orbital to spin moments, in the multilayers are 0.01 ± 0.01 for the Fe sites and 0.03 ± 0.01 for the Co.

IV. DISCUSSION

The orbital contribution to the magnetic moment in amorphous CoFeZr layers is dominated by Co, as described above. The relative weight of the orbital contribution is larger in Co compared to Fe, in their elemental composition. The m_{orbit}/m_{spin} were previously determined using XMCD to be 0.043 and 0.095 for Fe and Co, respectively.[18] Furthermore, the m_{orbit}/m_{spin} is heavily affected by alloying; in $Fe_{67}Co_{33}$ these are 0.098 and 0.217 for Fe and Co, respectively.[19] Thus the orbital momentum of both Fe and Co is doubled by alloying, as compared to their elemental values whereas the spin moments are more modestly affected.

In the CoFeZr alloys discussed here, the orbital contribution to the moment is suppressed for both Fe and Co. This is somewhat expected, as the ternary alloy is amorphous and therefore exhibits no long-range crystalline order. The resulting orbital to spin ratio of Co was determined to be 0.078 ± 0.005 which is surprisingly close to what is obtained for pure crystalline Co (0.095). Thus, the absence of long-range order appears to have a minute influence on the orbit to spin ratio of the Co moment. The suppression of the orbit to spin ratio in Fe is much larger, from 0.043 to 0.012 ± 0.005. The suppression of the orbital moment is much more profound in Fe than Co when compared to their elemental crystalline structures. The differences in the degree of quenching

cannot be due to differences in the local configuration of the atoms as they are random and expected to be similar for both Fe and Co, as seen in the similarity of the element-specific magnetization loops (Fig. 8). A strong contribution from the electronic part is therefore anticipated. Calculations of the influence of both the order and the alloying is therefore important for understanding these differences. There are currently no calculations available for these important material parameters in amorphous alloys.

The m_{orbit}/m_{spin} contribution diminishes strongly for both Fe and Co, when the CoFeZr layers are decreased in thickness. This is apparent from the results obtained on the CoFeZr/AlZr multilayers. The m_{orbit} to m_{spin} ratio is decreased to 0.01 ± 0.01 for the Fe atoms and 0.03 ± 0.01 for the Co, in the 30/30 multilayer. The contribution from the hybridization of the ferromagnetic layer with the nonmagnetic layers is likely to be important in this perspective, however the strength of this proximity effect is surprising. Intermixing is evident from the microscopy and x-ray data in all the samples which could amplify the effect. However, a firm conclusion depends on more complementary experiments or theoretical calculations.

The Fe and Co are strongly coupled and can therefore be treated as having magnetic properties which are the weighted average of the two constituents. While the addition of Fe increases the magnetic moment of the material, the orbital contribution is decreased. Thus, the current measurements give a good understanding of the influence of Fe on the magnetic properties of amorphous CoFeZr alloys. The addition of Fe decreases the coercivity, resulting in softening of the magnetic properties,[20] due to the decrease in the effective orbital contribution to the moment.

In the amorphous alloys that we have presented, the absence of crystalline order is apparently not sufficient to remove the orbital contribution to the moment. Thus, it is conceivable that local atomic configurations causes the observed anisotropy in amorphous materials with the subsequent spin-orbit coupling being the underlying cause of the magnetic anisotropy. Under normal growth conditions the configurational anisotropy is completely random, due to the randomness of the atomic order. However, field-induced anisotropy has been known for quite a while in Co-rich magnetic amorphous materials.[21–23] Furthermore, the anisotropy can even be imprinted layer by layer in amorphous multilayers by the selection of the applied external field.[4] Thus the formation of a macroscopic *easy axis* is possible, which must be related to the local configuration of the magnetic atoms. This configurational variation is most likely associated with small differences in the nearest-neighbor distances and composition.[6,24] The length scales of these differences are out of reach for most structural measurements. The term configurational anisotropy is therefore appropriate, when describing the anisotropy in amorphous materials.

V. CONCLUSION

The m_{orbit} to m_{spin} ratio of elemental Co is only modestly decreased by forming amorphous CoFeZr alloys. The corresponding changes in Fe are much larger. Thus, the effective m_{orbit} to m_{spin} ratio can be adjusted by the Fe to Co ratio, allowing tailoring of the magnetic anisotropy in amorphous CoFeZr alloys. Anisotropy cannot be treated as uniquely coupled to periodic lattices and the term crystalline anisotropy is therefore misleading. The magnetic anisotropy in amorphous materials must be viewed as a local property, associated with the orbital contribution from atomic configurations and a corresponding local magnetostrictive field. Configurational anisotropy is therefore a more appropriate term when addressing the magnetic anisotropy in amorphous materials. The configurational anisotropy is a local property, which can even be aligned by applying an external field during growth.

ACKNOWLEDGMENTS

The authors would like to acknowledge the support from the Swedish Research Council (VR) and Knut and Alice Wallenberg Foundation (KAW).

*bjorgvin.hjorvarsson@fysik.uu.se

[1] D. Djayaprawira, K. Tsunekawa, M. Nagai, H. Maehara, S. Yamagata, N. Watanabe, S. Yuasa, Y. Suzuki, and K. Ando, Appl. Phys. Lett. **86**, 092502 (2005).
[2] J.-O. Song and S.-R. Lee, J. Magn. Magn. Mater. **310**, 1923 (2007).
[3] G. Suran, F. Machizaud, and M. Naili, Phys. Rev. B **47**, 15007 (1993).
[4] H. Raanaei, H. Nguyen, G. Andersson, H. Lidbaum, P. Korelis, K. Leifer, and B. Hjörvarsson, J. Appl. Phys. **106**, 023918 (2009).
[5] Y. Imry and S.-K. Ma, Phys. Rev. Lett. **35**, 1399 (1975).
[6] R. Harris, M. Plischke, and M. J. Zuckermann, Phys. Rev. Lett. **31**, 160 (1973).
[7] J. McCord, I. Monch, J. Fassbender, A. Gerber, and E. Quandt, J. Phys. D **42**, 055006 (2009).
[8] J. McCord, T. Gemming, L. Schultz, J. Fassbender, M. O. Liedke, M. Frommberger, and E. Quandt, Appl. Phys. Lett. **86**, 162502 (2005).
[9] A. T. Hindmarch, C. J. Kinane, M. MacKenzie, J. N. Chapman, M. Henini, D. Taylor, D. A. Arena, J. Dvorak, B. J. Hickey, and C. H. Marrows, Phys. Rev. Lett. **100**, 117201 (2008).
[10] P. Carra, B. T. Thole, M. Altarelli, and X. Wang, Phys. Rev. Lett. **70**, 694 (1993).
[11] B. T. Thole, P. Carra, F. Sette, and G. van der Laan, Phys. Rev. Lett. **68**, 1943 (1992).
[12] S. Pizzini, L. M. García, A. Fontaine, J. P. Rueff, J. Vogel, R. M. Galéra, J. B. Goedkoop, N. B. Brookes, G. Krill, and J. P. Kappler, J. Electron Spectrosc. Relat. Phenom. **86**, 165 (1997).
[13] J. Vogel, M. Sacchi, R. J. H. Kappert, J. C. Fuggle, J. B. Goedkoop, N. B. Brookes, G. van der Laan, and E. E. Marinero, J. Magn. Magn. Mater. **150**, 293 (1995).

[14] S. Imada, T. Muro, S. Suga, K. Kobayashi, H. Maruyama, and H. Yamazaki, J. Electron Spectrosc. Relat. Phenom. **78**, 279 (1996).
[15] C. Bordel, S. Pizzini, J. Vogel, K. Mackay, J. Voiron, R. M. Galéra, A. Fontaine, P. Auric, J. B. Goedkoop, and N. B. Brookes, Phys. Rev. B **56**, 8149 (1997).
[16] A. R. B. de Castro, G. B. Fraguas, P. T. Fonseca, R. N. Suave, S. Gama, A. A. Coelho, and I. A. Santos, J. Electron Spectrosc. Relat. Phenom. **101-103**, 725 (1999).
[17] M. Björck and G. Andersson, J. Appl. Crystallogr. **40**, 1174 (2007).
[18] C. T. Chen, Y. U. Idzerda, H.-J. Lin, N. V. Smith, G. Meigs, E. Chaban, G. H. Ho, E. Pellegrin, and F. Sette, Phys. Rev. Lett. **75**, 152 (1995).
[19] L. Zong-Mu, X. Fa-Qiang, W. Li-Wu, W. Jie, Z. Jun-Fa, and Z. Wen-Hua, Chin. Phys. Lett. **24**, 2667 (2007).
[20] G. Suran, M. Naili, H. Niedoba, F. Machizaud, O. Acher, and D. Pain, J. Magn. Magn. Mater. **192**, 443 (1999).
[21] G. Suran, K. Ounadjela, J. Sztern, and C. Sella, J. Appl. Phys. **55**, 1757 (1984).
[22] G. Suran, J. Sztern, and B. Barbara, Appl. Phys. Lett. **58**, 1338 (1991).
[23] V. G. Harris, K. D. Aylesworth, B. N. Das, W. T. Elam, and N. C. Koon, Phys. Rev. Lett. **69**, 1939 (1992).
[24] X. Yan, M. Hirscher, T. Egami, and E. E. Marinero, Phys. Rev. B **43**, 9300 (1991).